Experiments in fluids manuscript No.
(will be inserted by the editor)

Application of short-range dual-Doppler lidars to evaluate the coherence of turbulence

Etienne Cheynet · Jasna Bogunović Jakobsen · Jónas Snæbjörnsson · Torben Mikkelsen · Mikael Sjöholm · Jakob Mann · Per Hansen · Nikolas Angelou · Benny Svardal

Received: date / Accepted: date

Abstract Two synchronized continuous wave scanning lidars are used to study the coherence of the along-wind and across-wind velocity components. The goal is to evaluate the potential of the lidar technology for application in wind engineering. The wind lidars were installed on the Lysefjord Bridge during four days in May 2014 to monitor the wind field in the horizontal plane upstream of the bridge deck. Wind records obtained by five sonic anemometers mounted on the West side of the bridge are used as reference data. Single and two-point statistics of wind turbulence are studied, with special emphasis on the root-coherence and the co-coherence of turbulence. A four-parameter decaying exponential function has been fitted to the measured co-coherence and a good agreement is observed between data obtained by the sonic anemometers and the lidars. The root-coherence of turbulence is compared to theoretical models. The analytical predictions agree rather well with the measured coherence for the along-wind component. For increasing wavenumbers, larger discrepancies are however noticeable between the measured coherence and the theoretical predictions. The WindScanners are observed to slightly overestimate the integral length scales, which could not be explained by the laser beam averaging effect alone. On the other hand, the spatial averaging effect does not seem to have any significant effect on the coherence.

Keywords Full scale measurement · Long-span bridge · Wind lidars · Turbulence · Coherence.

Etienne Cheynet · Jasna Bogunović Jakobsen · Jonas Snæbjörnsson
Department of Mechanical and Structural Engineering and Materials Science, University of Stavanger, N-4036 Stavanger, Norway
E-mail: etienne.cheynet@uis.no

Jonas Snæbjörnsson
School of Science and Engineering, Reykjavik University, Menntavegur 1, 101 Reykjavk, Iceland

Torben Mikkelsen · Mikael Sjöholm · Jakob Mann · Per Hansen · Nikolas Angelou
Department of Wind Energy, Technical University of Denmark, Risø Campus Frederiksborgvej 399, DK-4000 Roskilde, Denmark

Benny Svardal
Christian Michelsen Research AS, Fantoftveien 38, Bergen, Norway

1 Introduction

The deployment of a single Doppler wind lidar to study atmospheric turbulence is limited by the fact that only the along-beam wind velocity is recorded. To retrieve the three wind components, a system of triple lidars is necessary (Mikkelsen et al 2008a,b; Mann et al 2009). If only two of the wind components are of interest, a dual-lidar system can be used instead. That type of system was for example used in combination with sonic anemometers by Calhoun et al (2006) to obtain the vertical profile of horizontal wind velocity created by the intersection of two Range Height Indicator (RHI) scans. If the goal is to recover the along-wind and across-wind components, dual Plan Position Indicator (PPI) scans with low elevation angles can be used (Newsom et al 2008).

A review of the estimation of the turbulence statistics by Sathe and Mann (2013) showed that wind lidars have mainly been used in two domains: wind energy and atmospheric research. For the latter, Reitebuch (2012) has provided a short review. For wind energy applications, wind lidars have mainly been used for wind profiling (Peña et al 2009), to investigate the flow variability in complex terrain (Barkwith and Collier 2011; Lange et al 2015), in studies of atmospheric stability (Friedrich et al 2012), wind turbulence (Sathe et al 2011), the flow upstream (Simley et al 2016) or downstream of a single (Iungo et al 2013) or multiple (Kumer et al 2015) wind turbines.

The application of multiple wind lidars in civil engineering is appealing because of their potential to study two-point statistics of wind turbulence. Among them, the coherence

is of particular interest. The coherence describes the spatial correlation of wind gusts in the frequency domain. Full-scale measurements of the wind coherence are fundamental to accurately estimate the total wind load acting on large structures such as long-span suspension bridges (Toriumi et al 2000; Miyata et al 2002) or wind turbines (Saranyasoontorn et al 2004).

The characterization of wind coherence for lateral separations has previously been obtained from arrays of met-masts (Ropelewski et al 1973; Kristensen and Jensen 1979) but their deployment in complex terrain or in offshore environments may not be easy. The installation of an array of sonic anemometers along the deck of a long-span bridge is an alternative (Toriumi et al 2000; Miyata et al 2002) that remains rarely used. Firstly because the instrumentation of a long-span bridge is cumbersome and secondly because such structures are not always available. The deployment of dual wind lidars may become an alternative to accurately measure wind coherence in a near future.

The study of wind coherence with lidars has been little documented so far. By using a single pulsed Doppler lidar and the zenith-pointing mode in flat terrain, Lothon et al (2006) measured the coherence of the vertical wind component along the scanning beam. At that time, Lothon et al (2006) did not find similar studies in the literature that could be compared with their results. Kristensen et al (2010) conducted another analysis of the along-beam coherence by using a single wind lidar, for different angles between the mean wind direction and the beam orientation. In a proof-of-concept study, Cheynet et al (2016b) used a single pulsed wind lidar to monitor the lateral and vertical coherence for the along-wind component in offshore environment, but were limited to the case where the wind direction was more or less aligned with the scanning beam. Motivated by its relevance for the wind loading on slender structures, the present study focuses on the coherence of the horizontal wind components along a line segment, measured by a dual-lidar system.

In this pilot study, continuous wave (CW) lidars are used to study atmospheric turbulence along the span of a suspension bridge. The short-range WindScanner system (`http://www.windscanner.dk/`) developed at the Department of Wind Energy at the Technical University of Denmark (DTU) Risø campus is used for this purpose. The present paper aims to evaluate the ability of the WindScanners to measure the coherence of the horizontal wind components for lateral separations. In addition, we aim to evaluate the relative importance of the lidar spatial averaging effect on the accuracy of turbulence measurement.

The WindScanner system was deployed on the deck of the Lysefjord Bridge during four days in May 2014. The bridge has been instrumented with multiple sonic anemometers that have been measuring the wind field continuously since November 2013. The relatively low wind velocity recorded during the WindScanners deployment period resulted in a low availability of the data. The present study therefore demonstrates the suitability of lidars to measure spectral coherence rather than characterizing the turbulence at the bridge site with statistical significance. In the following, the particular scanning pattern of the lidar is first described as well as the positions of anemometers along the bridge span. The single-point statistics of atmospheric turbulence are then analysed, followed by a comparison of the coherence measurements obtained by the anemometers and the lidars. The discussion focuses on the influence of the non-stationarity of the wind data and the volume averaging effect of the lidar data on turbulence measurements.

Fig. 1: East view of the Lysefjord Bridge site.

2 Measurement site and instrumentation

The Lysefjord Bridge crosses the narrow inlet of a fjord in the South-West coast of Norway (Fig. 1). Its main span is 446 m long and its centre stretches 55 m above the sea level. The bridge is entrenched between steep hills and high mountains, i.e. immersed in a flow strongly influenced by the topography. Two prevailing wind directions are commonly observed at the bridge site and correspond to flows from S-SW and N-NE which display different turbulent characteristics (Cheynet et al 2016a). The flow from N-NE comes from the nearby mountains or follows the fjord over a longer path. On the other hand, the flow from S-SW comes from a more open and levelled area.

2.1 The sonic anemometry

In November 2013, four 3D WindMaster Pro sonic anemometers from Gill Instrument Ltd were deployed on the West side

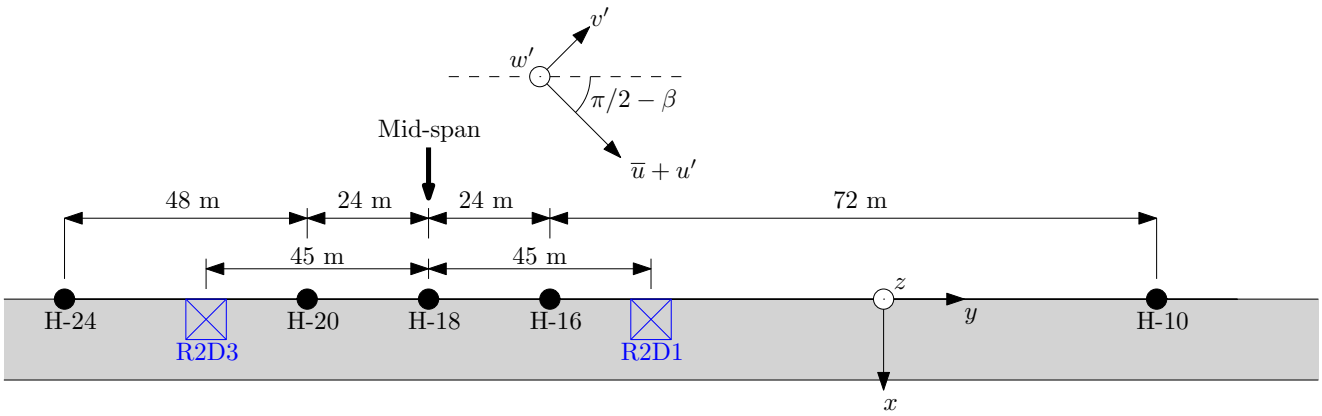

Fig. 2: Schematic of the bridge deck and its coordinate system with the anemometers (black dots) and the WindScanners R2D1 and R2D3 (symbols: ⊠) installed on the deck West side. The angle between the wind direction and the normal to the deck is called "yaw angle" and denoted β in the following.

of the deck on hangers 16, 18, 20 and 24, referred to as H-16, H-18, H-20 and H-24 respectively (Fig. 2). In addition, a Vaisala weather transmitter WXT520 was fixed to hanger 10, denoted H-10. These five anemometers are installed 6 m above the deck and are fixed either directly on the hangers or on poles supported by the main cables (Fig. 3). The anemometer data are sampled at 20 Hz. On 2014-05-22, the five sonic anemometers were continuously recording the along-wind, across-wind and vertical wind velocity components, denoted u, v, and w respectively. The along-wind component is split up into a mean part, $\overline{u}$, and a fluctuating part with zero mean, u':

$$u = \overline{u} + u' \quad (1)$$

$$v = \overline{v} + v' \quad (2)$$

$$w = \overline{w} + w' \quad (3)$$

where $\overline{v} = \overline{w} = 0\,\mathrm{m\,s^{-1}}$ (Teunissen 1980).

2.2 Wind conditions

Wind conditions observed on 2014-05-22 are summarized in Fig. 4, in terms of mean wind velocity, turbulence intensity and mean wind direction, where all data points are based on records of 10 min duration. In the morning, up to 12:20, the wind direction was N-NE with a wind velocity lower than 8 $\mathrm{m\,s^{-1}}$. Between 11:20 and 12:00, the wind direction switched to S-SW and remained the same until the next day. The mean wind velocity reached its maximum between 16:00 and 18:00, which is the period in which the turbulence data discussed hereafter were recorded. During that period, the mean wind direction fluctuated between 180° and 195°. For this wind sector, a rather high turbulence intensity was recorded, probably because the approaching flow crosses over hilly landscapes and the change of terrain roughness due

Fig. 3: WindScanner R2D1 (top) aiming at the South-West side of the Lysefjord Bridge, and sonic anemometers (bottom panels) installed above the bridge deck.

to the sea-land discontinuity occurs relatively close to the bridge deck. As pointed-out by Antonia and Luxton (1972), the evolution of the turbulence intensity for a roughness change from rough-to-smooth may not be monotonically

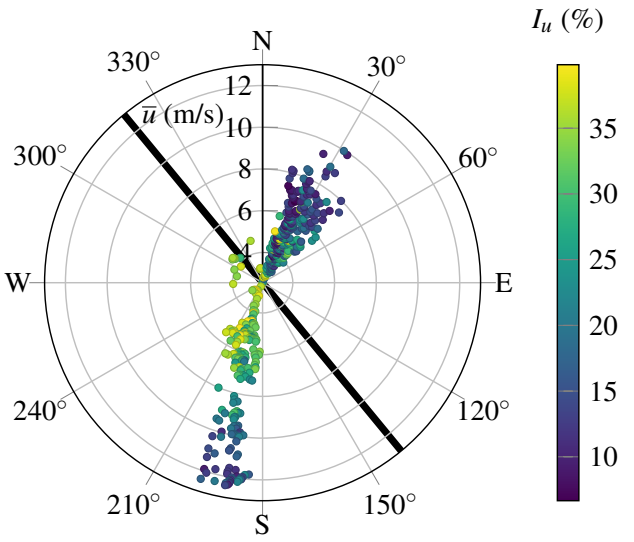

Fig. 4: Mean wind direction, velocity and turbulence intensity of the along-wind component on 2014-05-22. The bridge axis (thick solid line) makes an angle of 40° with the North.

decreasing and larger turbulence intensity can therefore be expected in the vicinity of a roughness change such as the one South of the Lysefjord Bridge.

2.3 The WindScanner system

The short-range WindScanner system is based on synchronized coherent continuous wave (CW) wind lidar instruments, which are actually a modified version of the ZephIR 150 (Natural Power) equipped with a 3 inches (7.62 cm) optical lens. The principles of CW lidar is described by (Karlsson et al 2000), while a description of the particular short-range WindScanner used in this study is given by Sjöholm et al (2014). The configuration of the WindScanners used here is summarized in Table 1. It is almost the same as described in Mann et al (2010), the main difference being that the lidars used in the present study have a more versatile rotating scanning head allowing a scan within a cone with a half opening angle of 60°.

The laser transmitter of the lidar operates at a wavelength of 1.565 µm, with an along-beam sampling frequency of 390 Hz. The along-beam wind component is recorded based on the Doppler frequency shift of the backscattered light from aerosols present in the atmosphere, using heterodyne detection technique. Sjöholm et al (2014) have previously used a similar configuration to characterize the rotorcraft downwash flow of a helicopter in a vertical and horizontal plane and were able to map the mean flow with good spatial resolution. Recently, Lange et al (2015) applied the WindScanner system to study the wind field in a complex terrain along several

Table 1: Configuration of the lidar instruments used in the present study.

Properties	Short-range WindScanner
Wavelength	1565 µm
Beam-width (at 40 m range)	< 1 mm
Shortest range	10 m
Longest range	< 200 m
Scan line sweep frequency	1 Hz
Scan line sweep length	123 m
Line-of-sight (LOS) sampling frequency	390 Hz
Lidars LOS detection range	$\pm$ 18 m s^{-1}

vertical line segments. In the present study, the scan is carried out in the horizontal plane only.

2.3.1 *Beam sweeping mode*

When the beam-sweeping mode is used, the two lidars denoted R2D3 and R2D1 in Fig. 5 aim at the same point 40 m upstream of the deck. By synchronized steering of the measurement location, the WindScanners scan continuously the area along a 123 m line segment parallel to the bridge deck and centred on H-18. The continuously acquired measurements along the line are in the post processing discretized into 26 segments, with a mean spatial resolution of 5 m except at the end points where the resolution is 3.7 m and 4.3 m, respectively. The pattern drawn by the intersection of the two scanning beams is almost a triangular waveform when displayed as a function of the time, except for the turning points which are rounded for a smooth motor motion (Fig. 6).

The scanning beam needs 0.5 s to travel along the 123 m line segment. At the centre of the scanned line, the sampling frequency is uniformly 2 Hz while towards the ends it alternates between a short and a long sampling separation (Fig. 6). The transformation of the non-uniform sampling frequency into a uniform one is therefore a preliminary step that must be carried out before analysing the wind velocity data. The upper limit of the spectral analysis of the wind data is therefore fixed to 0.5 Hz. The choice of a Nyquist frequency of 0.5 Hz is governed by the largest sampling time for the lidar data, which is 1 s.

For a zero elevation angle, the along-beam velocity is first expressed as a function of the wind components normal and along the bridge deck, denoted v_x and v_y respectively. The angles between the deck axis and the orientation of the beams are α_1 and α_2 for the WindScanner R2D1 and R2D3 respectively (Fig.5). For two synchronized wind lidars, the across-wind and along-wind components can be retrieved using a two-step procedure inspired from algorithms previously proposed by Newsom et al (2008) and applied by e.g. Stawiarski et al (2013) and Newsom et al (2015). Firstly, the

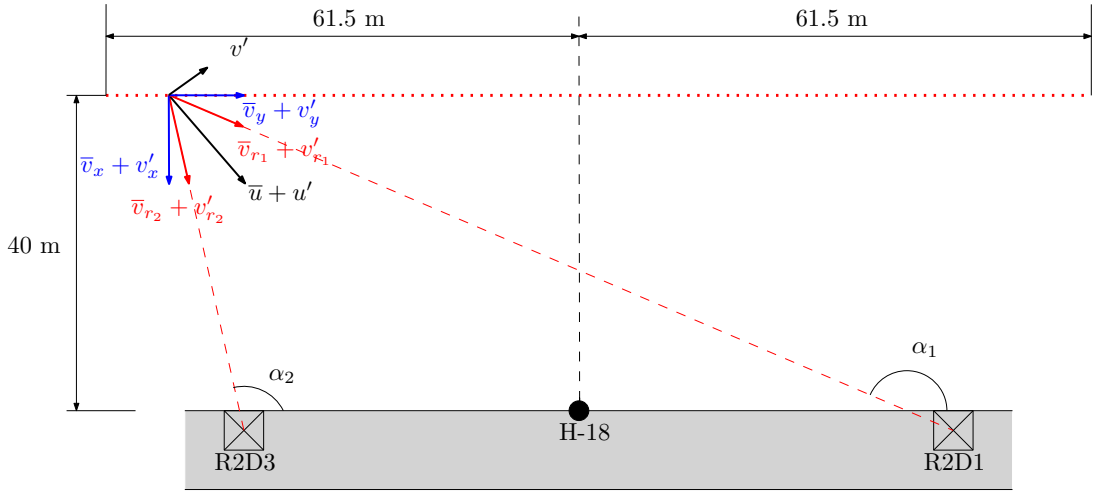

Fig. 5: Schematic of the dual-lidar system with the along-wind and across-wind components (black), the along-span and across-span components (blue), and the along-beam wind component (red).

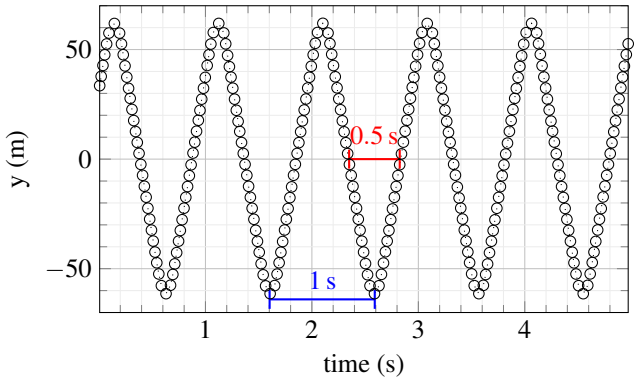

Fig. 6: Trajectory followed by the intersection of the two scanning beams of the WindScanners. Each circle represents one volume analysed at a given time step.

wind components v_x and v_y are obtained using:

$$\begin{bmatrix} v_x \\ v_y \end{bmatrix} = \mathbf{M}^{-1} \begin{bmatrix} v_{r_1} \\ v_{r_2} \end{bmatrix} \tag{4}$$

where:

$$\mathbf{M} = \begin{bmatrix} \sin(\alpha_1) & -\cos(\alpha_1) \\ \sin(\alpha_2) & -\cos(\alpha_2) \end{bmatrix} \tag{5}$$

Secondly, the wind components u and v are calculated using the yaw angle β:

$$\begin{bmatrix} u \\ v \end{bmatrix} = \begin{bmatrix} \cos(\beta) & \sin(\beta) \\ -\sin(\beta) & \cos(\beta) \end{bmatrix} \cdot \begin{bmatrix} v_x \\ v_y \end{bmatrix} \tag{6}$$

where:

$$\beta = \arctan\left(\frac{v_y}{v_x}\right) \tag{7}$$

2.3.2 *The spatial averaging effect*

Contrary to sonic anemometers that are essentially monitoring the flow in a volume small enough to be considered as a point for wind engineering applications, Doppler wind lidars measure the wind velocity in a volume stretched along the beam, in which the high-frequency wind components are "smoothened" out to a certain degree. This results in an attenuated spectrum at high frequencies for the along-beam wind velocity in comparison to the wind spectrum from the sonic anemometers (Sjöholm et al 2008, 2009; Angelou et al 2012).

Following Smalikho (1995), the low-pass filter effect can be expressed as a convolution between the spatial averaging function ϕ and the vector of the wind velocity $\mathbf{v_r^0}$ projected along the beam at a focus distance r from the lidar:

$$\mathbf{v_r}(r) = \int_{-\infty}^{+\infty} \phi(s)\mathbf{n} \cdot \mathbf{v_r^0}(s\mathbf{n} + r\mathbf{n})\,\mathrm{d}s \tag{8}$$

Here $\mathbf{n}$ is a unit vector along the beam and s is the distance along the beam from the measured point. When the beam is aligned with the wind direction, Eq. 8 can be directly calculated using a scalar convolution product. The function ϕ can be approximated by a Lorentzian function (Sonnenschein and Horrigan 1971):

$$\phi(s) = \frac{1}{\pi} \frac{Z_r}{Z_r^2 + s^2} \tag{9}$$

where Z_r is the Rayleigh length defined as:

$$Z_r = \frac{\lambda r^2}{2\pi a_0^2} \tag{10}$$

where $\lambda = 1.565\,\mu\mathrm{m}$ is the wavelength of the laser source and $a_0 \approx 20\,\mathrm{mm}$ is the beam radius.

The range-resolution of a CW lidar is expressed by its Full Width at Half Maximum (FWHM), which is approximatively equal to two times the Rayleigh length (Mikkelsen 2009). As shown in Eq. 10, the FWHM increases quadratically with the measurement distance. Consequently, a constant spatial resolution along the laser beams cannot be achieved in the present case because the scanning distance to the WindScanners is varying. The focus distances measured here range from 40 m to ca. 114 m, i.e. the FWHM fluctuates between 2.0 m and 16.6 m.

The spectral transfer function $\mathbf{H}$ associated with Eq. 9 is therefore expressed as a function of the distance r and the wavenumber k:

$$|\mathbf{H}(k,r)|^2 = e^{-2Z_r|k|} \tag{11}$$

If the scanning beam is aligned with the mean wind direction, the spectrum of the filtered radial velocity $\mathbf{S}_{v_r}$ is:

$$\mathbf{S}_{v_r}(k) = |\mathbf{H}(k,r)|^2 \cdot \mathbf{S}^0_{v_r}(k) \tag{12}$$

If the scanning beam is not aligned with the wind direction, Eq. 8 must be solved considering the three dimensional structure of wind turbulence. Then the spectral transfer function depends on three variables: the distance r, the wavenumber k and the angle θ between the beam and the wind direction. This does not allow a simple analytical expression of the spectral transfer function, except for the case of isotropic turbulence in the inertial subrange (Kristensen et al 2011).

3 Single and two-point statistics

The data from the anemometers and the CW lidars are synchronized using GPS time. For the time series considered, the gust front recorded 40 m upstream to the deck needs ca. 4 s to reach the bridge position, based on the mean wind velocity of the flow. Because the integral time scale measured by the anemometers was larger than 11 s, we used Taylor's hypothesis of frozen turbulence to assume that the wind data recorded 40 m upstream to the deck differs from those along the deck by a time lag only. The time lag was estimated using a cross correlation between the wind velocity recorded by the sonic anemometer on H-18 and the WindScanners and was equal to about 4 s.

3.1 Integral length scales

The streamwise turbulence length scales or integral length scales are calculated based on the integration to the first zero crossing of the auto-covariance of the wind velocity components as proposed by e.g. Lenschow and Stankov (1986). The integral time scale T_i, where $i = \{u,v\}$ refers to the along-wind and across-wind components respectively, is first calculated. Taylor's hypothesis of frozen turbulence is then applied to estimate the integral length scale L_i:

$$T_i = \int_{t=0}^{t(R_i(t)=0)} R_i(t)\,\mathrm{d}t \tag{13}$$

$$L_i = \overline{u} \cdot T_i \tag{14}$$

where $\overline{u}$ is the horizontal mean wind velocity component recorded at a single point, and R_i is the auto-covariance function of the fluctuating wind velocity.

3.2 Spectral analysis

The power spectral densities (PSD) of the wind velocity data are calculated using Welch's overlapped segment averaging estimator (Welch 1967) and bin averaged using a logarithmic spaced abscissa. A record of 20 min duration is used and divided into overlapping segments of 10 min with 50% overlapping as suggested by Carter et al (1973). The frequency band ranges therefore from 1.67 mHz to 0.5 Hz.

3.3 Root-coherence and co-coherence

The root-coherence is defined in Eq. 15 using the same notations as Davenport (1961). It is expressed as the normalized cross-spectral density of the wind fluctuations measured simultaneously at two different positions y_p and y_q along the bridge deck:

$$\gamma_{pq}(f) = \sqrt{\mathbf{Co}^2_{pq}(f) + \mathbf{Qu}^2_{pq}(f)} \tag{15}$$

in which $\mathbf{Co}_{pq}$ and $\mathbf{Qu}_{pq}$ are the co-coherence and quad-coherence of the velocity fluctuations respectively, defined for a given frequency f, and a spatial separation $d_y = |y_p - y_q|$ as:

$$\mathbf{Co}_{pq}(f) = \mathrm{Re}\left(\frac{\mathbf{S}_{pq}(f)}{\sqrt{\mathbf{S}_p(f)\cdot\mathbf{S}_q(f)}}\right) \tag{16}$$

$$\mathbf{Qu}_{pq}(f) = \mathrm{Im}\left(\frac{\mathbf{S}_{pq}(f)}{\sqrt{\mathbf{S}_p(f)\cdot\mathbf{S}_q(f)}}\right) \tag{17}$$

where $\mathbf{S}_{pq}$ is the cross-spectral density of the velocity fluctuations recorded at the positions y_p and y_q. In the following, the root-coherence function is denoted γ_u and γ_v for the along-wind and across-wind components respectively. The application of the root-coherence to estimate wind loads on structures was first introduced by Davenport (1961, 1962) for vertical separations, then generalized by Vickery (1970) for both lateral and vertical separations. To consider the in-phase correlation of the wind load only, the co-coherence defined in Eq. 16 is used, as illustrated by early works from e.g. Panofsky and Singer (1965) or Shiotani and Iwatani (1971). In the

present paper, the root-coherence and the co-coherence are studied separately.

The root coherence is calculated for the along-wind and across-wind components in the cross-flow direction. The cross-flow separation, denoted D, is obtained by projection of the bridge axis segment in question onto the line perpendicular to the flow in a similar fashion as done by Saranyasoontorn et al (2004). For the calculation of the co-coherence, instantaneous wind measurements for different cross-flow separations are required. Unfortunately, the wind direction was not normal to the deck during the period studied. For a mean wind direction of 190°, a non-negligible yaw angle of 40° between the wind direction and the normal to the deck is recorded. Consequently, we hereby present the co-coherence for the wind component normal to the deck axis. This allows a comparison between the data from the WindScanners and the anemometers, but not a direct comparison with the characteristics of the along-wind turbulence reported in the literature.

The coherence is calculated based on 10 min of wind data recorded between 16:25:00 and 16:35:00 on 2014-05-22. To reduce the measurement noise and the bias of the coherence spectrum estimate, the root-coherence and co-coherence are computed using overlapping segments of 1 min each via Welch's method and 50% overlapping, leading to recorded data at frequencies ranging from 16.7 mHz to 0.5 Hz. With a larger data set, we can increase the length of the overlapping segment to improve the frequency resolution, and keep the measurement noise and the bias low. The co-coherence and root-coherence are calculated for all possible combinations of lateral separations, and the average over identical distances is calculated. The measured co-coherence is approximated in the least-square sense by a four-parameter exponential decay function inspired by e.g. Hjorth-Hansen et al (1992) and Jakobsen (1997):

$$\mathrm{Co}(d_y,f)=\exp\left\{-\left[\frac{d_y}{\overline{v}_x}\sqrt{(c_1 f)^2+c_2^2}\right]^{c_3}\right\}\cos\left(c_4\frac{d_y f}{\overline{v}_x}\right) \tag{18}$$

where $\overline{v}_x$ is the mean wind velocity normal to the deck and c_1, c_2, c_3, c_4 are coefficients to be determined.

The measured root-coherence is compared to two theoretical models. The first one is the von Kármán isotropic coherence model (von Kármán 1948) which is defined for the along-wind and across-wind components as:

$$\gamma_u(f)=A\cdot\left[K_{5/6}(\eta)-\frac{1}{2}\eta K_{1/6}(\eta)\right] \tag{19}$$

$$\gamma_v(f)=A\cdot\left[K_{5/6}(\eta)+\frac{3n^2}{3\eta^2+5n^2}\eta K_{1/6}(\eta)\right] \tag{20}$$

where η, A and n are:

$$A=\frac{2}{\Gamma(\frac{5}{6})}\left(\frac{\eta}{2}\right)^{5/6} \tag{21}$$

$$\eta=\sqrt{n^2+(D/L)^2} \tag{22}$$

$$n=\frac{2\pi f D}{\overline{u}}=kD \tag{23}$$

According to ESDU 86010 (2001), the isotropic integral length scale L is defined as $L=2L_u$, where L_u is here calculated using Eqs. 13-14. Γ is the gamma function and K_i is the modified Bessel function of the second kind (Luke 1962).

The second model is a modified von Kármán coherence model provided by ESDU 86010 (2001). For a given cross-flow separation D, it is defined for the along-wind and across-wind components as:

$$\gamma_u(f)=\exp\left(-1.15\eta_1^{1.5}\right) \tag{24}$$

$$\gamma_v(f)=\exp\left(-0.65\eta_1^{1.3}\right) \tag{25}$$

where :

$$\eta_1=\sqrt{(0.747r)^2+(cn)^2} \tag{26}$$

$$r=\frac{D}{2L_u^c} \tag{27}$$

$$c=\max\left(1,\frac{1.6r^{0.13}}{\eta^b}\right) \tag{28}$$

$$b=0.35r^{0.2} \tag{29}$$

$$L_u^c=2L_u\left\{1-0.46\exp\left[-35(z/h)^{1.7}\right]\right\} \tag{30}$$

$$h=\frac{1}{6}u_*\cdot 10^4 \tag{31}$$

where η and n are defined in Eq. 22 and Eq. 23 respectively. L_u^c is the length scale of the along-wind turbulence in the cross-flow direction. It is expressed as a function of the altitude z of the anemometers and the height h of the boundary layer, expressed as a function of the friction velocity u_* and equal to 358 meter in the present study.

4 Stationarity test

To assess the stationarity of the wind velocity data recorded, the reverse arrangement (RA) test (Bendat and Piersol 2011) is considered. This test has been previously applied to wind velocity data (Xu 2013; Wang et al 2016) and more generally to a variety of random processes, see e.g. Aryan et al (2013); Beck et al (2006). According to Bendat and Piersol (2011), the RA test is a "non-parametric and distribution-free procedure where no assumption is made concerning the probability distribution of the data being evaluated" used to detect non-negligible trends in a random data set. By paraphrasing Siegel and Castellan (1988), the null hypothesis

for this test is that the wind sample considered is made of independent observations. The alternative hypothesis is that the data points are not random because of the existence of an underlying trend.

Consider a sample $X = \{X_1, X_2, ...X_N\}$ made of N data points corresponding to the along-wind velocity component. According to Bendat and Piersol (2011), a reverse arrangement is defined as the number of times that $X_i > X_j$ for $i < j$. For a number A of reverse arrangements, the mean and standard deviation of A are:

$$\mu_a = \frac{N(N-1)}{4} \tag{32}$$

$$\sigma_a = \frac{N(2N+5)(N-1)}{72} \tag{33}$$

Following Siegel and Castellan (1988), a z-score is calculated as:

$$z = \frac{A - \mu_a}{\sqrt{\sigma_a}} \tag{34}$$

In the following, the null hypothesis is verified at 5% significance level if $-1.96 \leq z \leq 1.96$.

5 Results

5.1 Wind field mapping

The high spatial and temporal resolution of the dual-lidar system allows a mapping of the wind field along a 123-m long line segment parallel to the deck (Fig. 7). The largest gusts are seen to appear systematically along the entire monitored domain and are skewed with respect to the bridge deck orientation, which indicates a non-zero yaw angle for the wind direction.

A more detailed comparison of the recorded velocity data between the anemometer on H-18 and the WindScanner 40 m upstream to the bridge, at a lateral distance of 2 m from H-18 is shown in Fig. 8. A good agreement is obtained between the data from the anemometers and the WindScanners. The last 5 min of the record show a sudden decrease of the wind velocity for both the along-wind and across-wind components. Such variations are rather common at the Lysefjord Bridge site and are often associated with slight changes in the mean flow direction, as indicated in the bottom panel of Fig. 8. In this particular case, wind from S-SW implies that the bridge becomes sheltered by the terrain in the South and so exposed to lower wind velocities. This may be interpreted as non-stationary wind fluctuations (cf. subsection 5.4), which are likely to be responsible for an overestimation of the turbulent length scales and the turbulence intensities (Chen et al 2007; Wang et al 2016). Similar large variations are noticeable during the first 5 min of the time series corresponding to the across-wind component and the wind direction.

5.2 Uniformity of the flow along the deck

The along-span variations of the integral length scales L_u and L_v, the horizontal mean wind velocity $\overline{u}$, the standard deviations σ_u and σ_v and the mean wind direction are presented in Fig. 9. The anemometer and WindScanner measurements are compared to investigate the capability of the CW lidars used in the present study to capture single-point statistics of atmospheric turbulence. The abscissa is defined as the distances varying from 0 m to 168 m, corresponding to the distance between the anemometers at H-10 and H-24.

The values of L_u and L_v data are particularly large for both the anemometers and the WindScanners. In addition, the dual-lidar system seems to systematically measure larger integral length scales than those obtained with the anemometers. We suspect the beam averaging effect to be responsible for the overestimation, i.e. the smoothing of the high frequency content of the data leads to an auto-correlation function that decays more slowly with the time lag.

The mean wind velocity $\overline{u}$ recorded by the WindScanners shows a good overall agreement with the one measured by the anemometers near mid-span (hangers 16 to 20), but a larger difference is observed with the value recorded by the sonic on H-24. The discrepancy between the data from the anemometers and the WindScanners is however on average lower than 3% for the mean wind velocity, which is acceptable. Peña et al (2009) has used a similar profiling CW lidar in offshore environment and found a coefficient of determination R^2 higher than 0.95 between the horizontal mean wind speed recorded by cup anemometers and the lidar. Although the lidar device measures slightly lower values than the anemometers for σ_u and σ_v, a rather good agreement is obtained. However, Peña et al (2009) observed a larger discrepancy between the standard deviation of the horizontal wind components measured by the anemometers and the wind lidar. One must note that Peña et al (2009) used a Velocity-Azimuth Display (VAD) scanning mode which was shown by Sathe et al (2011) to have limited capacities to accurately measure atmospheric turbulence.

Both the anemometers and the WindScanners measure a uniform wind direction near the central part of the deck. Near hangers 10 and 24, the anemometer data show a certain variation in the wind direction, which may be due to slight differences in the alignment of the sensors or the influence of the topography on the wind direction near the towers.

5.3 Overestimation of the integral length scale by the WindScanners

To investigate the influence of the spatial averaging effect on the estimation of the integral length scales, the case where the along-beam component recorded by the WindScanner R2D1 with an angle $\alpha_1 = 128°$ between 16:20 and 16:40

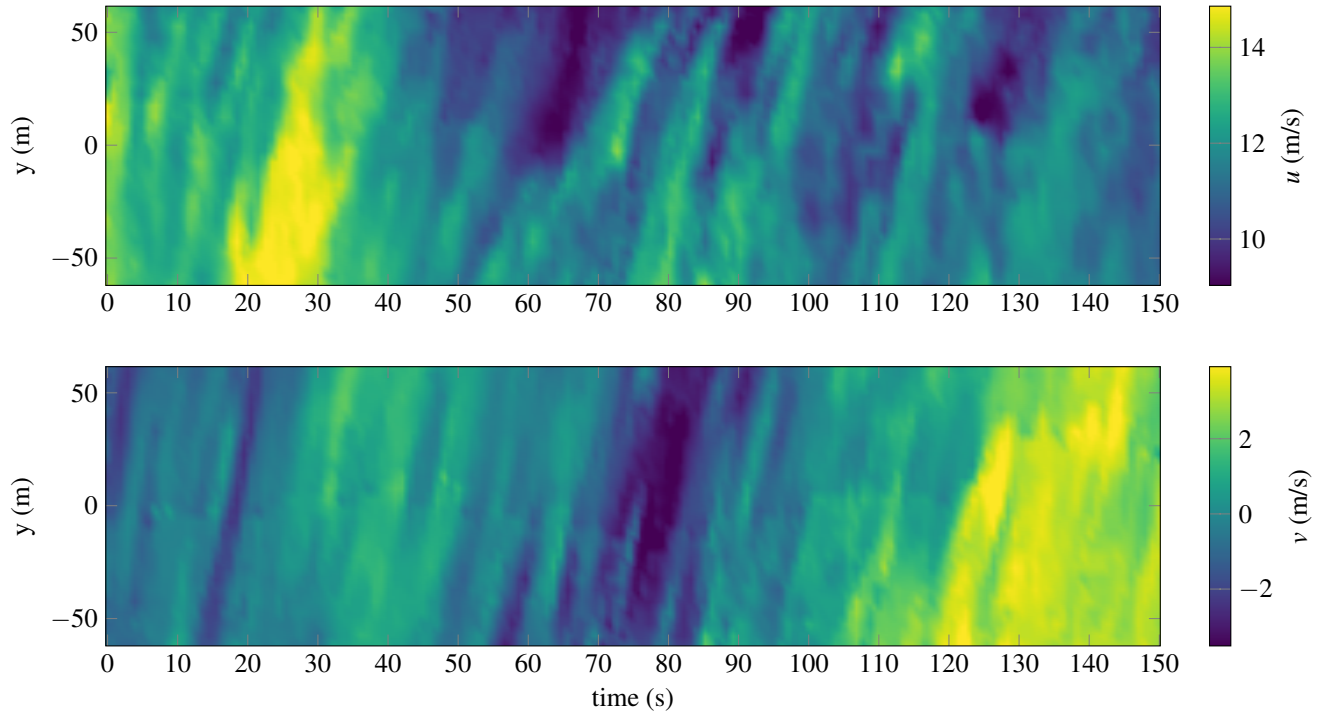

Fig. 7: Along-wind (top) and across-wind components (bottom) recorded by the WindScanners from 16:20 on 2014-05-22.

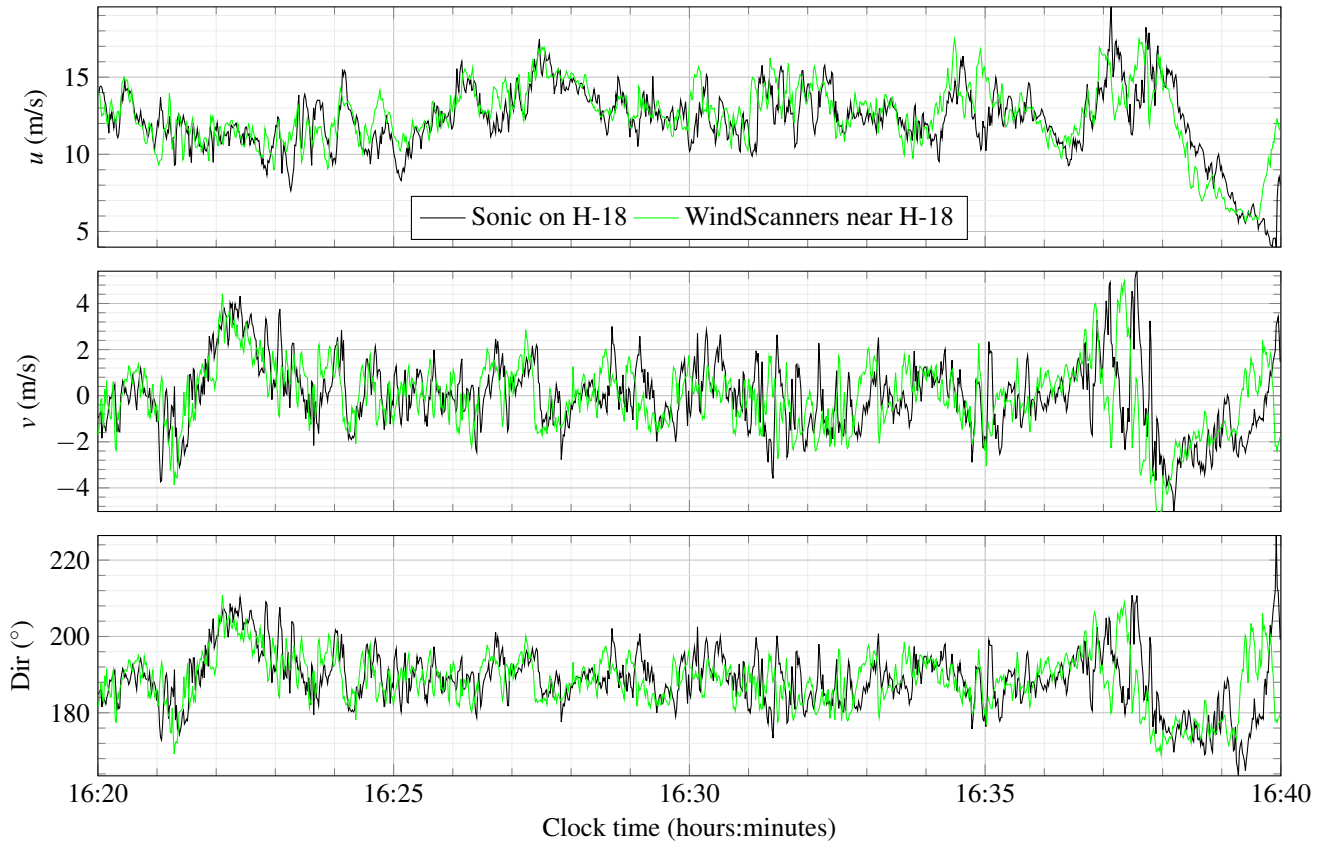

Fig. 8: Along-wind (top), across-wind components (middle) and wind direction (bottom) measured by the WindScanners and the anemometers near hanger 18, on 2014-05-22, after synchronization of the records.

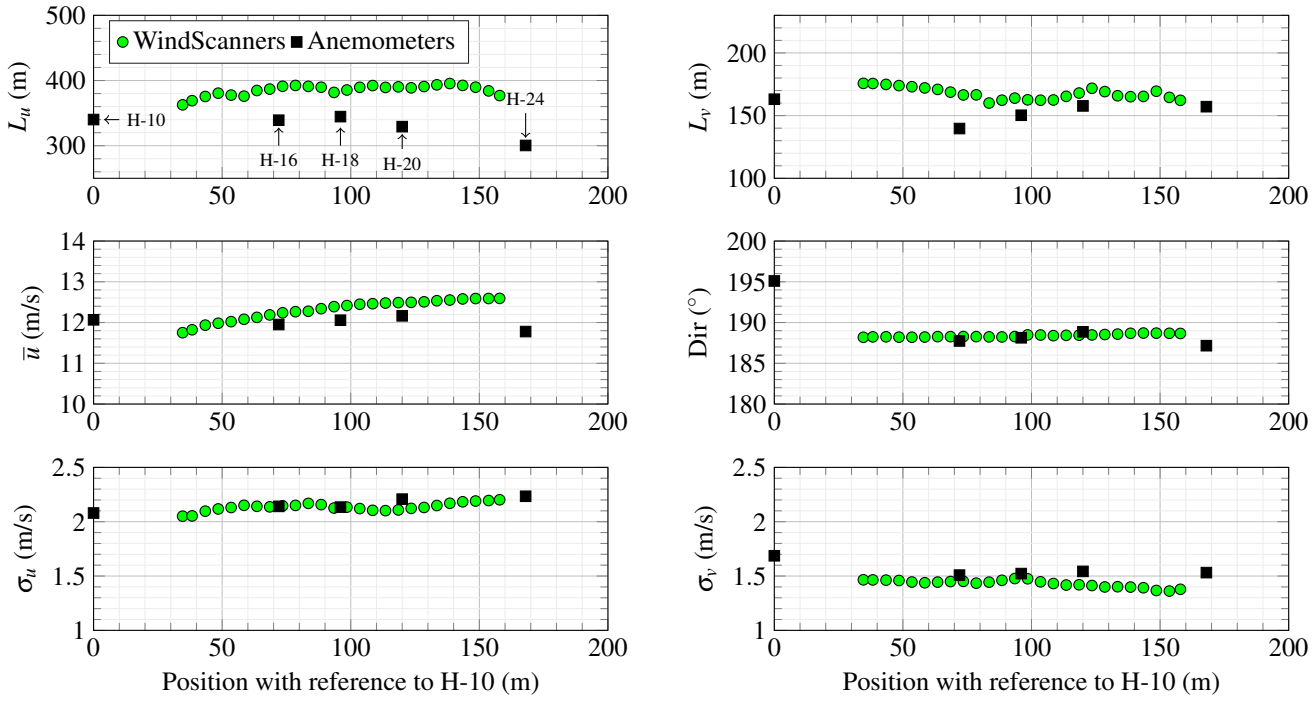

Fig. 9: Single-point statistics of atmospheric turbulence measured by the WindScanners and the anemometers along the bridge deck on 2014-05-22 between 16:20 and 16:40.

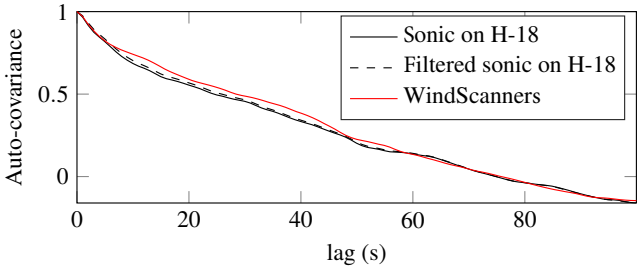

Fig. 10: Auto-covariance function for the along-wind component calculated at mid-span for wind data recorded from 16:20 to 16:40 on 2014-05-22, with and without introducing spatial averaging.

on 2014-05-22 is considered. Under this configuration, the focus distance r, is around 51 m and the beam is aligned with the measured mean wind direction. Eqs. 8-11 are then applied to introduce the spatial averaging on the along-beam velocity component recorded by the anemometer on H-18. The auto-covariance function of the filtered and unfiltered along-wind component is compared to the auto-covariance function measured by the WindScanner R2D1 in Fig. 10.

In this subsection, the integral time scale is considered instead of the integral length scale to avoid the introduction of an additional discrepancy due to the slightly different mean wind velocity measured by the WindScanners and the anemometer on H-18. The integral time scale for the WindScanner data is 31.7 s whereas it is 28.8 s and 29.4 s for the unfiltered and the filtered along-wind component measured by the anemometer on H-18. This leads to a difference of 10 % between the WindScanners and the unfiltered anemometer data. The difference increases to 13 % if Eq. 14 is used because of the discrepancy that already exists between the value of $\overline{u}$ estimated by the WindScanners and the anemometers. The anemometers measure a more heterogeneous along-span distribution of the integral length scales than the WindScanners, leading to an increased discrepancy between the anemometer and WindScanner estimates when the integral length scales L_u are averaged along the deck span.

As seen in Fig. 10, the spatial averaging effect introduced leads to a slight increase of the estimated integral time scales. However, it does not fully explain the discrepancies between the WindScanner and the anemometer estimates. The calculation of the integral length scales was done in the present study by using both WindScanners, which results in a more complex spatial averaging that cannot be simply expressed analytically. In addition, the spatial filtering in the transverse direction due to the beam motion was not modelled here and may lead to an increased measurement error. As pointed out by Stawiarski et al (2015), additional sources of discrepancies such as data aggregation and weighting in the lidar data retrieval process, are likely to be present. Finally, a minor difference between the flow conditions 40 m upstream of the

bridge and those observed 6 m above the bridge deck may also result in different length scales.

5.4 Influence of non-stationary wind fluctuations

Large streamwise turbulence length scales have been predicted by Hui et al (2009a) for the Stonecutter bridge with values for L_u and L_v equal to 378 m and 125 m respectively. Based on 10 min averaged data, a long-term monitoring campaign conducted by Wang et al (2013) showed that these length scales could fluctuate from couple of metres to more than 1 km. The measured turbulence length scales shown in Fig. 9 correspond to integral time scales above 25 s, which are considerably larger than those usually recorded at the Lysefjord Bridge site, which range from 10 s to 15 s. As underlined by Chen et al (2007), the calculation of the streamwise and cross-flow turbulence length scales should be done with caution for non-stationary flows.

In the present case, wind conditions during the first and the last 5 min of the data discussed are different from those in the remaining part of the time-series and thus introduce a non-stationarity of the overall record. Fig. 11 shows results from the reverse arrangement (RA) test based on wind data recorded from 16:20 to 16:40 (top panel) and from 16:25 to 16:35 (bottom panel).

For the RA test used here, the sampling frequency was decimated to 0.5 Hz, which explains why the maximal number of observations is equal to 600 for a wind record of 20 min duration. On the top panel of Fig. 11, the z-score falls outside the acceptance range for almost every observation whereas in the bottom panel of Fig. 11, the z-score falls within the acceptance range after ca. 150 observations which suggests a more stationary flow.

Because a more stationary flow is recorded between 16:25 and 16:35, the single-point statistics of wind turbulence are calculated again for this period. Table 2 summarizes the values found by the anemometers and the WindScanners, as well as the relative differences calculated, with respect to the anemometers measurements. When 10 min of wind data is considered, the WindScanners and anemometers measure much lower turbulence length scales than in the initial case where 20 min of wind data is used. For an averaging period of 10 min, the ratio between the across-wind and along-wind turbulence intensities I_v/I_u is 0.72 and 0.79 for the WindScanners and the anemometers respectively. These ratios are realistic according to the review of Solari and Piccardo (2001), but are slightly lower than those obtained during more recent measurement campaigns on long-span bridges site by e.g. Hui et al (2009b) or Wang et al (2013). For the present case and the single-point statistics studied, it was generally found that the deviation between the data from anemometers and the WindScanners was relatively stable. However, additional WindScanner data is needed to be included to provide statistical significance.

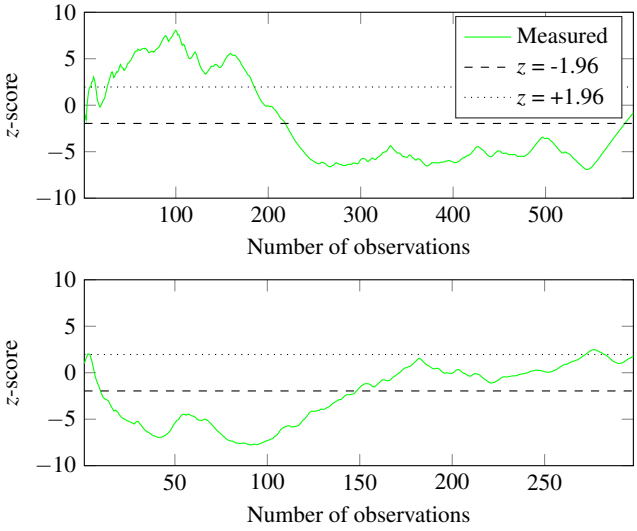

Fig. 11: RA test applied to wind data recorded by the anemometer on H-18, on 2014-05-22 between 16:20 and 16:40 (top) and between 16:25 and 16:35 (bottom). Outside the 95 % confidence level (dashed and dotted lines), the flow is non-stationary.

5.5 Co-coherence

In Fig.12, the scatter plot shows the co-coherence measured by the WindScanners and the anemometers for the wind component v_x and for three different values of d_y. The four-parameter decaying exponential function is fitted to the measured co-coherence and represented by solid lines. The fitted function captures relatively well the negative part of the measure co-coherence, which justifies the introduction of the parameter c_4 in Eq. 18.

The fitted coefficients for the WindScanners and the anemometers are presented in Table 3, and are of the same order of magnitude for both the along-wind and the across-wind components. According to Saranyasoontorn et al (2004), the computation of the co-coherence should be done based on records divided into overlapping segments of 75 s to 300 s. Herein, overlapping segments of 60 s are used to improve the readability of the subplots in figures 12. For verification purposes, the fitting process was repeated using a co-coherence measured based on overlapping segments of 120 s. Insignificant differences were observed for the estimation of the coefficients c_1 to c_4, and the initial choice of 60 s overlapping segments is therefore maintained.

Despite the limited length of data used, the good agreement between the WindScanners and the anemometers suggests that the WindScanners can properly capture the co-

Table 2: Single-point statistics of wind turbulence measured by the WindScanners (WS) and the sonic anemometers (SA).

	Measurements				Relative difference (%)	
Period	16:25 to 16:35		16:20 to 16:40		16:25 to 16:35	16:20 to 16:40
Sensors	WS	SA	WS	SA	–	–
L_u (m)	180	140	385	331	29	17
L_v (m)	74	60	168	154	23	9.1
$\overline{u}$ ($\mathrm{m\,s^{-1}}$)	13.2	12.7	12.3	12.0	3.8	2.6
σ_u ($\mathrm{m\,s^{-1}}$)	1.38	1.47	2.14	2.16	-5.7	-1.1
σ_v ($\mathrm{m\,s^{-1}}$)	1.00	1.16	1.43	1.56	-14	-8.2
I_u (%)	10.5	11.6	17.3	18.0	-9.1	-3.6
I_v (%)	7.6	9.2	11.6	13.0	-18	-11

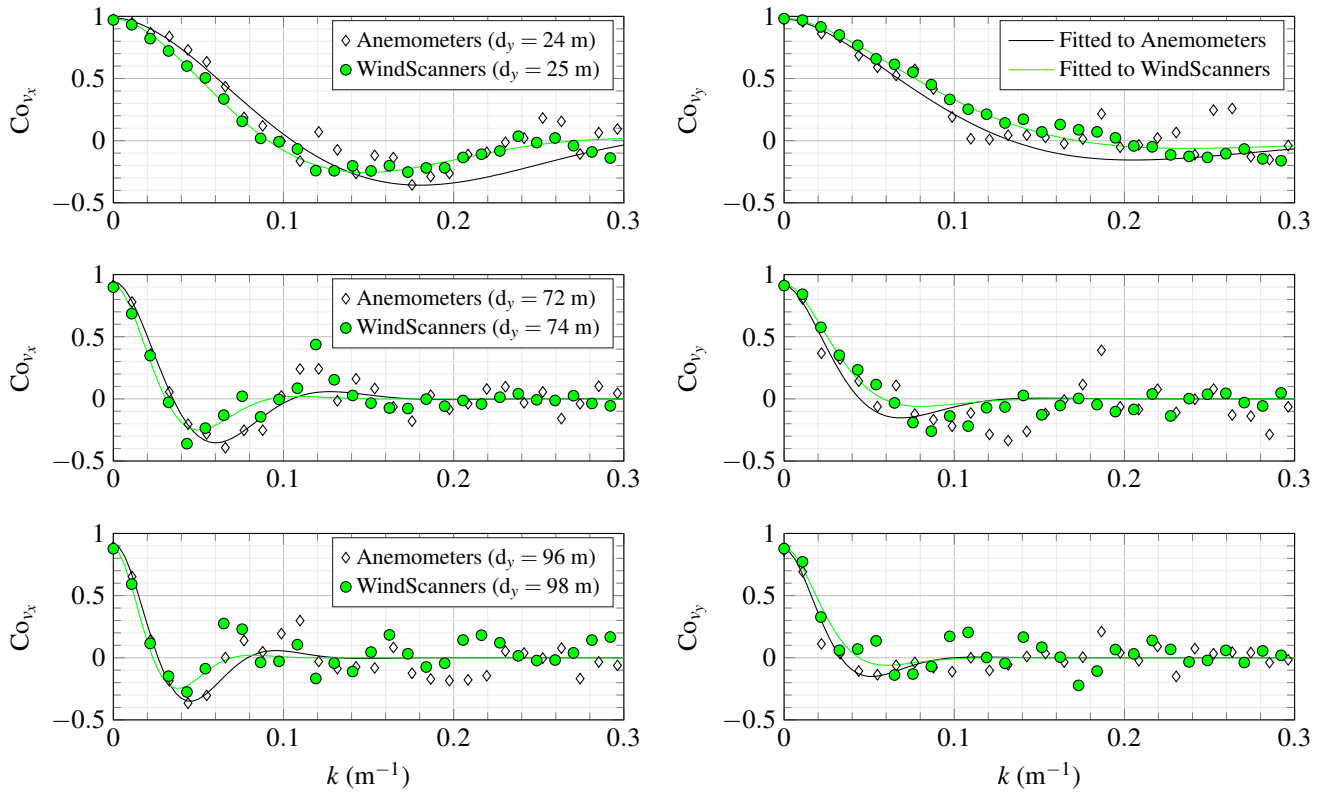

Fig. 12: Co-coherence measured (scatter plot) and fitted (solid lines) on 2014-05-22 between 16:25 and 16:35 for different separations along the deck span.

Table 3: Coefficients estimated with the four-parameter function for data recorded from 16:25 to 16:35 on 2014-05-22.

	Coefficients			
	c_1	c_2	c_3	c_4
Co_{v_x} (WindScanners)	1.9	0.02	1.4	4.3
Co_{v_x} (Anemometers)	1.4	0.02	1.4	3.9
Co_{v_y} (WindScanners)	1.8	0.02	1.5	2.3
Co_{v_y} (Anemometers)	1.8	0.02	1.4	3.1

coherence for the horizontal wind components. Larger data set should however be analysed to further validate the good agreement between the coherence measured by the anemometers and the one obtained with the WindScanners.

5.6 Root-coherence

The root-coherence is displayed for the horizontal wind components and for lateral separations ranging from ca. 18 m to 73 m in Fig. 13. It is expressed as a function of a non-dimensional wavenumber obtained by multiplying the wavenumber k with the crosswind separation D. The results based on the measured root-coherence from the WindScanners and the anemometers (scatter plot) are compared to theoretical

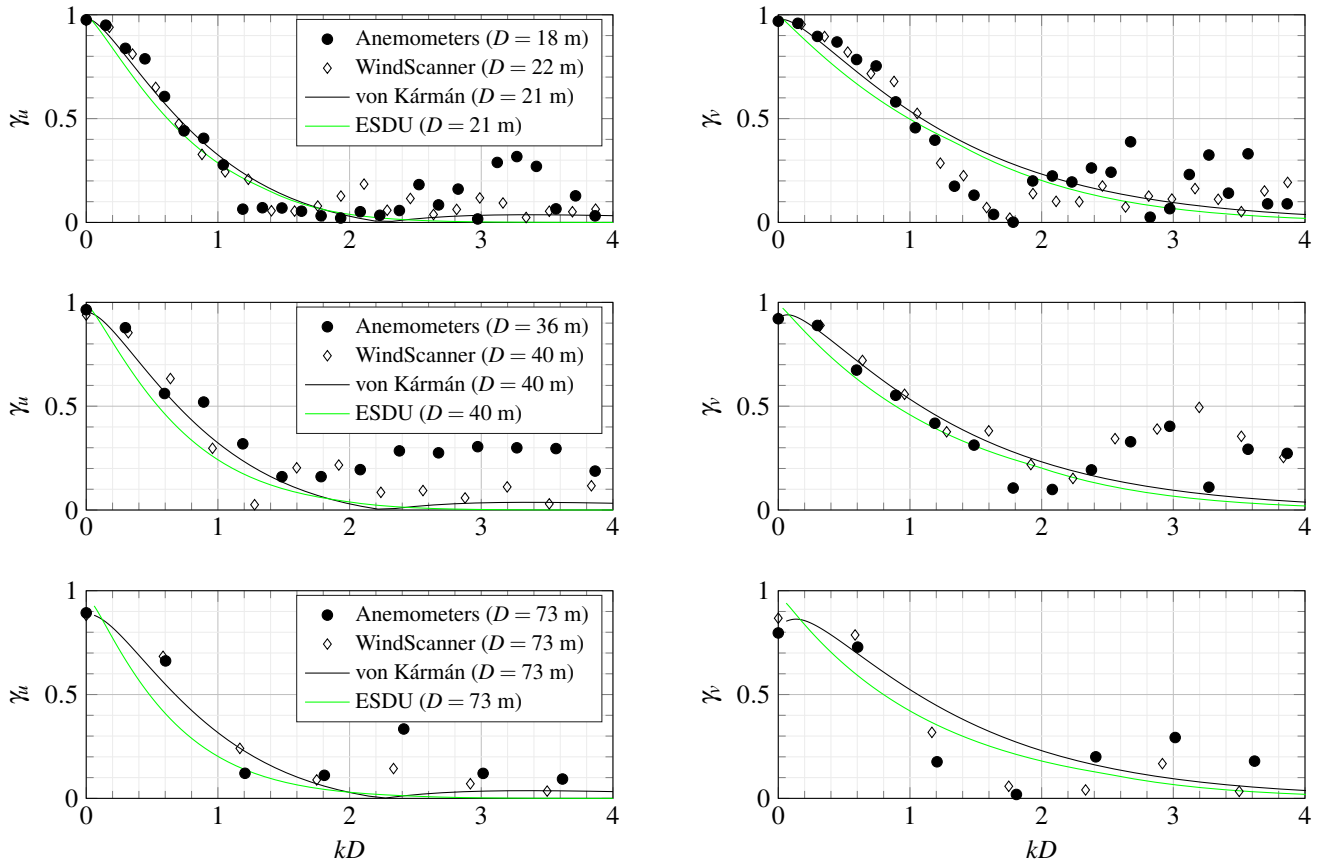

Fig. 13: Root-coherence for the along-wind (left) and across-wind components (right) from wind records on 2014-05-22 from 16:25 to 16:35.

root-coherence calculated with the von Kármán model and the ESDU model. A good agreement is visible between the anemometers and the WindScanners data for the different lateral separations presented.

For the along-wind component, the von Kármán model agrees fairly well the measured root-coherence, but gives larger values than the theoretical models for $kD > 2$. For the across-wind component, the measured root-coherence decreases faster than predicted.

The changing signs of the co-coherence function and the related positive values of the root-coherence function might be a signature of the particular coherent flow structures at the fjord inlet. Perhaps more likely, they are associated with the time lags by which the gust fronts arrive at different points along the measurements line upstream of the bridge. When the flow comes from S-SW with a yaw angle $\beta = 40°$, the distance between two points separated by e.g. $d_y = 72$ m along the measurement line (say points P_1 and P_2 as shown in Fig. 14) corresponds to a distance $d = 46$ m travelled in the along-flow direction. The distance is crossed in about 3.9 s at the mean wind speed of 12 m s^{-1}. For the velocity component with a period of 8 s, this corresponds to the out-

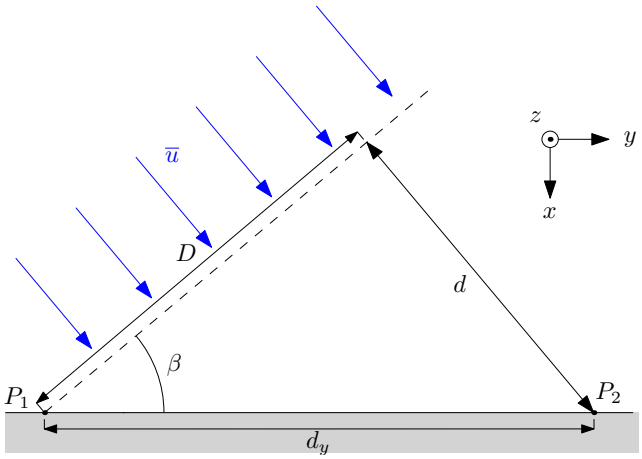

Fig. 14: Schematic of a skewed gust front arriving at point P_2 with a time delay $d/\overline{u}$ with respect to P_1.

of-phase variations, i.e. a systematic velocity increase at point P_1 and a simultaneous decrease at P_2, and a negative co-coherence. In the left panel of Fig. 12, this underpins a negative co-coherence value around $k = 0.065$ m^{-1} for

$d_y = 72$ m. Correspondingly, positive co-coherence has local culminations at about $2k$.

5.7 Influence of the spatial averaging effect on the coherence

Angelou et al (2012) compared the wind spectra obtained with one anemometer and one CW lidar located 67.5 m away, and the beam was aligned with the wind direction. Their results showed that the spatial averaging effect is low for wavenumbers below 0.1 m^{-1}, but becomes clearly visible for larger wavenumbers. In the present study, the wind spectra measured by the WindScanners and the anemometers in Fig. 15 agree rather well with the results from Angelou et al (2012), bearing in mind that the WindScanners used here have larger beam diameter emitted, i.e. smaller measurement volume at a given measurement range than the lidar used in the previous study.

On Fig. 15, the power spectral densities of the wind fluctuations evaluated based on data from anemometers and the WindScanners are directly compared for both the along-wind (top-left) and the across-wind components (top-right). The bottom-panels shows a comparison between the two wind components for the anemometers (bottom-left) and the WindScanners (bottom-right). The spatial averaging effect appears to be rather low for wavenumbers below 0.1 m^{-1} for the along-wind component and below 0.08 m^{-1} for the across-wind component. According to the bottom panels, a ratio close to $4/3$, as predicted by the Kolmogorov hypothesis for the inertial subrange is expected. Such a ratio was observed in flat and homogeneous terrain by e.g. Kaimal et al (1972), despite a non-negligible dependency on atmospheric stability. In the present study a ratio of 1.4 was obtained using the anemometer data for frequencies ranging from 1 Hz to 8 Hz. Such a comparison was not possible by using the WindScanner system, which in the particular scanning mode used, produces time series with a sampling frequency too low to accurately measure this ratio in the inertial subrange.

The wind coherence measured by the WindScanners is affected by the volume averaging effect, although Table 3 shows that the difference from the coherence based on the anemometer data remains small. There are two possible explanations for this. Firstly, the normalization of the cross-spectra reduces the spatial averaging effect. In a general case, the relation between the coherence and the spatial transfer function $\mathbf{H}$ is cumbersome to model because the latter depends both on the radial distance r and the angle θ between the beam and the wind direction. The spatial averaging effect can however be cancelled in a particular case, where two lidar beams are aligned with the flow, and monitor the wind field at two points y_1 and y_2, located at distances r_1 and r_2 from each lidar respectively. Under these conditions, analytic expressions of the single and two-point spectral densities of the wind components are much simpler, because they are not expressed as a combination of the different along-beam velocities:

$$\mathbf{S_u}(k,y_1) = |\mathbf{H}(k,r_1)|^2 \cdot \mathbf{S_u^0}(k,y_1) \tag{35}$$

$$\mathbf{S_u}(k,y_2) = |\mathbf{H}(k,r_2)|^2 \cdot \mathbf{S_u^0}(k,y_2) \tag{36}$$

$$\mathbf{S_u}(k,y_1,y_2) = \mathbf{H}^*(k,r_2) \cdot \mathbf{H}(k,r_1) \cdot \mathbf{S_u^0}(k,y_1,y_2) \tag{37}$$

where $\mathbf{H}^*$ is the conjugate of the spectral transfer function.

If $r_1 = r_2 = r$, then $\mathbf{H}$ becomes identical for the two along-beam wind velocities, and the root-coherence function becomes independent of the spectral transfer function:

$$\gamma_{\mathbf{u}}(y_1,y_2,k) = \frac{|\mathbf{S_u}(k,y_1,y_2)|}{\sqrt{\mathbf{S_u}(k,y_1)\cdot\mathbf{S_u}(k,y_2)}} \tag{38}$$

$$= \frac{|\mathbf{S_u^0}(k,y_1,y_2)|}{\sqrt{\mathbf{S_u^0}(k,y_1)\cdot\mathbf{S_u^0}(k,y_2)}} \tag{39}$$

The second reason that may explain why the averaging effect is hardly visible for the measured coherence is linked to the frequency range of interest. In Fig. 15, the spatial averaging effect for the along-wind component is rather low for wavenumbers below 0.1 m^{-1}, which is precisely the domain where the coherence is significantly high.

6 Conclusions

On 2014-05-22, horizontal turbulence was studied by a system of dual Doppler wind lidars (short-range WindScanners) installed on the main span of the Lysefjord Bridge. Measurements from sonic anemometers installed along the bridge span were used as reference data. The comparison of single-point and two-point statistics of wind turbulence aimed to investigate the applicability of dual-lidar systems to complement anemometers for the estimation of wind conditions relevant to structural design. A rather good agreement between data from the anemometers and the lidars was observed for the mean and standard deviation of the horizontal wind components. In the single case studied, the WindScanners overestimated the turbulence length scales, but the spatial averaging effect could not explain this overestimation alone. The difference was up to 29 % when 10 min of data are considered and 17 % when 20 min of wind data were used. A large amount of 10 min samples need to be considered for a more reliable estimation of this measurement error.

For the first time, the coherence has been measured for cross-flow separations by a dual-lidar system and compared to measurements from sonic anemometers. Encouraging results were obtained since the volume averaging effect cancels to a large degree when studying coherence. The measured coherence showed some discrepancies for $kD \geq 2$ compared to the values predicted by three different theoretical models. Anyway, a good overall agreement was observed between estimates based on data from anemometers and lidars.

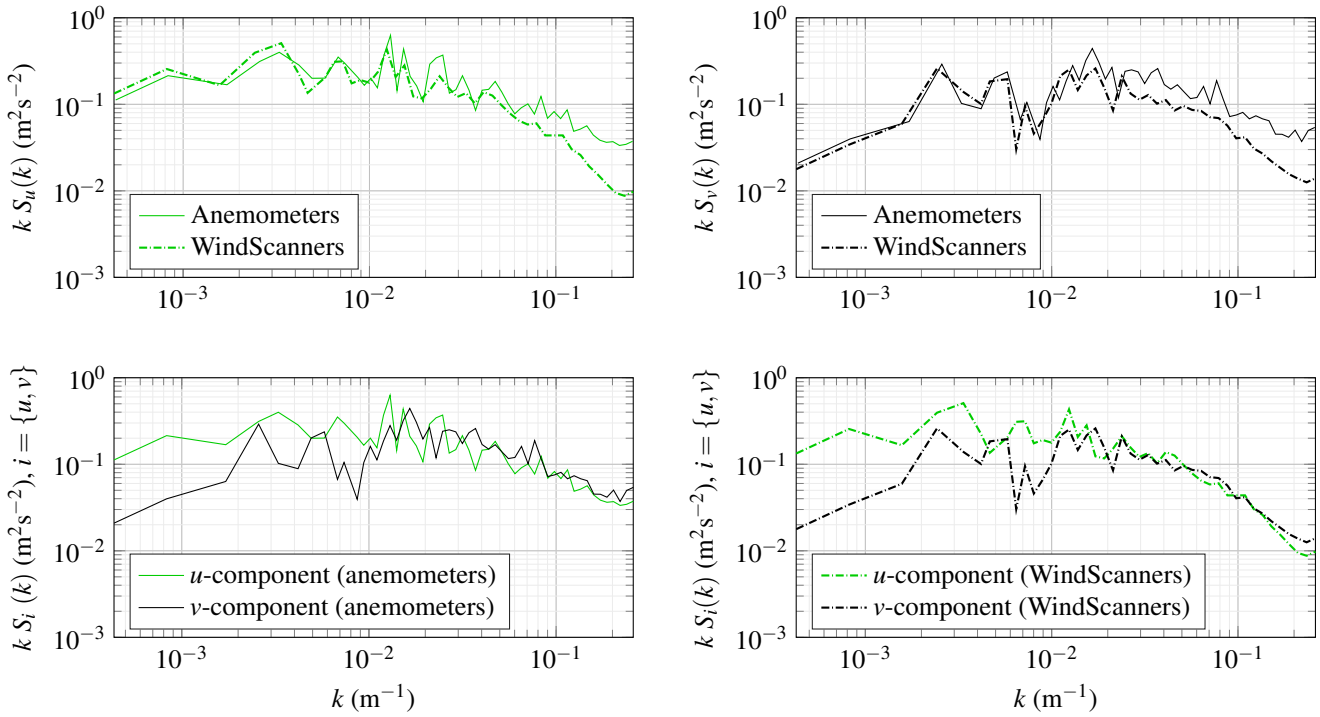

Fig. 15: PSD of the along-wind (top-left) and across-wind components (top-right) measured by the WindScanners and the anemometers, and direct comparison between S_u and S_v for the anemometers (bottom-left) and the WindScanners (bottom-right) is done using data recorded on 2014-05-22 between 16:20 and 16:40.

Because the present work is partly based on the analysis of a single wind record of 20 min, further studies should include a larger amount of samples to investigate atmospheric turbulence statistics. A short data set has however the advantage of allowing a relatively detailed comparison between the WindScanner system and sonic anemometers through an estimation of wind coherence. For a more complete assessment of the WindScanners performances, the vertical wind component should also be studied. Firstly because it plays a major role in the wind-induced vibrations of long-span bridges, and secondly because it would allow the evaluation of the capabilities of short-range WindScanners to capture the three-dimensional structure of wind turbulence.

Acknowledgements The study was initiated and performed with the support from The Norwegian Center for Offshore Wind Energy (NORCOWE, project number 193821 supported by the Research Council Norway).

References

Angelou N, Mann J, Sjöholm M, Courtney M (2012) Direct measurement of the spectral transfer function of a laser based anemometer. Review of Scientific Instruments 83(3):033111, DOI 10.1063/1.3697728

Antonia RA, Luxton RE (1972) The response of a turbulent boundary layer to a step change in surface roughness. Part 2. Rough-to-smooth. Journal of Fluid Mechanics 53, DOI 10.1017/S002211207200045X

Aryan H, Boynton RJ, Walker SN (2013) Analysis of trends between solar wind velocity and energetic electron fluxes at geostationary orbit using the reverse arrangement test. Journal of Geophysical Research: Space Physics 118(2):636–641, DOI 10.1029/2012JA018216

Barkwith A, Collier CG (2011) Lidar observations of flow variability over complex terrain. Meteorological Applications 18(3):372–382, DOI 10.1002/met.244

Beck TW, Housh TJ, Weir JP, Cramer JT, Vardaxis V, Johnson GO, Coburn JW, Malek MH, Mielke M (2006) An examination of the runs test, reverse arrangements test, and modified reverse arrangements test for assessing surface EMG signal stationarity. Journal of neuroscience methods 156(1):242–248, DOI 10.1016/j.jneumeth.2006.03.011

Bendat J, Piersol A (2011) Random Data: Analysis and Measurement Procedures. Wiley Series in Probability and Statistics, Wiley

Calhoun R, Heap R, Princevac M, Newsom R, Fernando H, Ligon D (2006) Virtual towers using coherent Doppler lidar during the Joint Urban 2003 dispersion experiment. Journal of Applied meteorology and climatology 45(8):1116–1126, DOI 10.1175/JAM2391.1

Carter G, Knapp C, Nuttall AH (1973) Estimation of the magnitude-squared coherence function via overlapped fast Fourier transform processing. Audio and Electroacoustics, IEEE Transactions on 21(4):337–344, DOI 10.1109/TAU.1973.1162496

Chen J, Hui M, Xu Y (2007) A comparative study of stationary and non-stationary wind models using field measurements. Boundary-Layer Meteorology 122(1):105–121, DOI 10.1007/s10546-006-9085-1

Cheynet E, Bogunović Jakobsen J, Snæbjörnsson J (2016a) Buffeting response of a suspension bridge in complex terrain. Engineering Structures 128:474–487, DOI 10.1016/j.engstruct.2016.09.060

Cheynet E, Bogunović Jakobsen J, Svardal B, Reuder J, Kumer V (2016b) Wind coherence measurement by a single pulsed Doppler wind lidar. Energy Procedia 94:462 – 477, DOI 10.1016/j.egypro.2016.09.217

Davenport AG (1961) The spectrum of horizontal gustiness near the ground in high winds. Quarterly Journal of the Royal Meteorological Society 87(372):194–211, DOI 10.1002/qj.49708737208

Davenport AG (1962) The response of slender, line-like structures to a gusty wind. Proceedings of the Institution of Civil Engineers 23(3):389–408, DOI 10.1680/iicep.1962.10876

ESDU 86010 (2001) Characteristics of atmospheric turbulence near the ground part III: variations in space and time for strong winds (neutral atmosphere). ESDU International

Friedrich K, Lundquist JK, Aitken M, Kalina EA, Marshall RF (2012) Stability and turbulence in the atmospheric boundary layer: A comparison of remote sensing and tower observations. Geophysical Research Letters 39, DOI 10.1029/2011gl050413

Hjorth-Hansen E, Jakobsen A, Strømmen E (1992) Wind buffeting of a rectangular box girder bridge. Journal of Wind Engineering and Industrial Aerodynamics 42, DOI 10.1016/0167-6105(92)90128-w

Hui M, Larsen A, Xiang H (2009a) Wind turbulence characteristics study at the Stonecutters Bridge site: Part II: Wind power spectra, integral length scales and coherences. Journal of Wind Engineering and Industrial Aerodynamics 97(1):48 – 59, DOI 10.1016/j.jweia.2008.11.003

Hui M, Larsen A, Xiang H (2009b) Wind turbulence characteristics study at the Stonecutters Bridge site: Part I:mean wind and turbulence intensities. Journal of Wind Engineering and Industrial Aerodynamics 97(1):22 – 36, DOI 10.1016/j.jweia.2008.11.002

Iungo GV, Wu YT, Porté-Agel F (2013) Field measurements of wind turbine wakes with lidars. Journal of Atmospheric and Oceanic Technology 30(2):274–287, DOI 10.1175/JTECH-D-12-00051.1

Jakobsen JB (1997) Span-wise structure of lift and overturning moment on a motionless bridge girder. Journal of wind engineering and industrial aerodynamics 69:795–805, DOI 10.1016/S0167-6105(97)00206-7

Kaimal JC, Wyngaard JC, Izumi Y, Cot OR (1972) Spectral characteristics of surface-layer turbulence. Quarterly Journal of the Royal Meteorological Society 98(417):563–589, DOI 10.1002/qj.49709841707

Karlsson CJ, Olsson FÅ, Letalick D, Harris M (2000) All-fiber multifunction continuous-wave coherent laser radar at 1.55 μm for range, speed, vibration, and wind measurements. Applied optics 39(21):3716–3726, DOI 10.1364/AO.39.003716

von Kármán T (1948) Progress in the statistical theory of turbulence. Proceedings of the National Academy of Sciences 34(11):530–539

Kristensen L, Jensen N (1979) Lateral coherence in isotropic turbulence and in the natural wind. Boundary-Layer Meteorology 17(3):353–373, DOI 10.1007/BF00117924

Kristensen L, Kirkegaard P, Mann J, Mikkelsen T, Nielsen M, Sjöholm M (2010) Spectral coherence along a lidar-anemometer beam. Tech. rep., Danmarks Tekniske Universitet, Risø Nationallaboratoriet for Bæredygtig Energi

Kristensen L, Kirkegaard P, Mikkelsen T (2011) Determining the velocity fine structure by a laser anemometer with fixed orientation. DTU Wind Energy E, DTU-Wind-Energy-E-0008(EN)

Kumer VM, Reuder J, Svardal B, Stre C, Eecen P (2015) Characterisation of single wind turbine wakes with static and scanning WINTWEX-W lidar data. Energy Procedia 80:245 – 254, DOI 10.1016/j.egypro.2015.11.428, 12th Deep Sea Offshore Wind R&D Conference, EERA DeepWind'2015

Lange J, Mann J, Angelou N, Berg J, Sjöholm M, Mikkelsen T (2015) Variations of the wake height over the Bolund escarpment measured by a scanning lidar. Boundary-Layer Meteorology pp 1–13, DOI 10.1007/s10546-015-0107-8

Lenschow DH, Stankov BB (1986) Length Scales in the Convective Boundary Layer. Journal of Atmospheric Sciences 43:1198–1209, DOI 10.1175/1520-0469(1986)043⟨1198:LSITCB⟩2.0.CO;2

Lothon M, Lenschow D, Mayor S (2006) Coherence and scale of vertical velocity in the convective boundary layer from a Doppler lidar. Boundary-Layer Meteorology 121(3):521–536, DOI 10.1007/s10546-006-9077-1

Luke YL (1962) Integrals of Bessel functions. McGraw-Hill

Mann J, Cariou JP, Courtney MS, Parmentier R, Mikkelsen T, Wagner R, Lindelöw P, Sjöholm M, Enevoldsen K (2009) Comparison of 3D turbulence measurements using three staring wind lidars and a sonic anemometer. Meteorologische Zeitschrift 18(2):135–140, DOI 10.1127/0941-2948/2009/0370

Mann J, Peña A, Bingöl F, Wagner R, Courtney M (2010) Lidar scanning of momentum flux in and above the atmospheric surface layer. Journal of Atmospheric and Oceanic Technology 27(6):959–976, DOI 10.1175/2010JTECHA1389.1

Mikkelsen T (2009) On mean wind and turbulence profile measurements from ground-based wind lidars: limitations in time and space resolution with continuous wave and pulsed lidar systems. In: European Wind Energy Conference and Exhibition 2009

Mikkelsen T, Courtney M, Antoniou I, Mann J (2008a) Wind scanner: A full-scale laser facility for wind and turbulence measurements around large wind turbines. In: European Wind Energy Conference and Exhibition 2008

Mikkelsen T, Mann J, Courtney M, Sjöholm M (2008b) Windscanner: 3-D wind and turbulence measurements from three steerable doppler lidars. IOP Conference Series: Earth and Environmental Science 1:U148–U156, DOI 10.1088/1755-1307/1/1/012018

Miyata T, Yamada H, Katsuchi H, Kitagawa M (2002) Full-scale measurement of Akashi–Kaikyo Bridge during typhoon. Journal of wind engineering and industrial aerodynamics 90(12):1517–1527, DOI 10.1016/S0167-6105(02)00267-2

Newsom R, Calhoun R, Ligon D, Allwine J (2008) Linearly organized turbulence structures observed over a suburban area by dual-Doppler lidar. Boundary-Layer Meteorology 127(1):111–130, DOI 10.1007/s10546-007-9243-0

Newsom RK, Berg LK, Shaw WJ, Fischer ML (2015) Turbine-scale wind field measurements using dual-Doppler lidar. Wind Energy 18(2):219–235, DOI 10.1002/we.1691

Panofsky HA, Singer IA (1965) Vertical structure of turbulence. Quarterly Journal of the Royal Meteorological Society 91, DOI 10.1002/qj.49709138908

Peña A, Hasager CB, Gryning SE, Courtney M, Antoniou I, Mikkelsen T (2009) Offshore wind profiling using light detection and ranging measurements. Wind Energy 12(2):105–124, DOI 10.1002/we.283

Reitebuch O (2012) Wind lidar for atmospheric research. In: Schumann U (ed) Atmospheric Physics, Research Topics in Aerospace, Springer Berlin Heidelberg, pp 487–507, DOI 10.1007/978-3-642-30183-4_30

Ropelewski CF, Tennekes H, Panofsky H (1973) Horizontal coherence of wind fluctuations. Boundary-Layer Meteorology 5(3):353–363, DOI 10.1007/BF00155243

Saranyasoontorn K, Manuel L, Veers PS (2004) A comparison of standard coherence models for inflow turbulence with estimates from field measurements. Journal of Solar Energy Engineering 126(4):1069–1082, DOI 10.1115/1.1797978

Sathe A, Mann J (2013) A review of turbulence measurements using ground-based wind lidars. Atmospheric Measurement Techniques 6(11):3147–3167, DOI 10.5194/amt-6-3147-2013

Sathe A, Mann J, Gottschall J, Courtney M (2011) Can wind lidars measure turbulence? Journal of Atmospheric and Oceanic Technology 28(7):853–868, DOI 10.1175/JTECH-D-10-05004.1

Shiotani M, Iwatani Y (1971) Correlations of wind velocities in relation to the gust loadings. In: Proceedings of the 3rd International Conference on Wind Effects on Buildings and Structures, Tokyo,

pp 57–67
Siegel S, Castellan N (1988) Nonparametric Statistics for the Behavioral Sciences. McGraw-Hill international editions. Statistics series, McGraw-Hill
Simley E, Angelou N, Mikkelsen T, Sjöholm M, Mann J, Pao LY (2016) Characterization of wind velocities in the upstream induction zone of a wind turbine using scanning continuous-wave lidars. Journal of Renewable and Sustainable Energy 8(1):013301, DOI 10.1063/1.4940025
Sjöholm M, Mikkelsen T, Mann J, Enevoldsen K, Courtney M (2008) Time series analysis of continuous-wave coherent Doppler lidar wind measurements. IOP Conference Series: Earth and Environmental Science 1(1):012,051, DOI 10.1088/1755-1315/1/1/012051
Sjöholm M, Mikkelsen T, Mann J, Enevoldsen K, Courtney M (2009) Spatial averaging-effects on turbulence measured by a continuous-wave coherent lidar. Meteorologische Zeitschrift 18(3):281–287, DOI doi:10.1127/0941-2948/2009/0379
Sjöholm M, Angelou N, Hansen P, Hansen KH, Mikkelsen T, Haga S, Silgjerd JA, Starsmore N (2014) Two-dimensional rotorcraft downwash flow field measurements by lidar-based wind scanners with agile beam steering. Journal of Atmospheric & Oceanic Technology 31(4):930 – 937, DOI 10.1175/JTECH-D-13-00010.1
Smalikho I (1995) On measurement of the dissipation rate of the turbulent energy with a CW Doppler lidar. Atmospheric and Ocean Optics 8:788–793
Solari G, Piccardo G (2001) Probabilistic 3-D turbulence modeling for gust buffeting of structures. Probabilistic Engineering Mechanics 16(1):73–86, DOI 10.1016/S0266-8920(00)00010-2
Sonnenschein CM, Horrigan FA (1971) Signal-to-noise relationships for coaxial systems that heterodyne backscatter from the atmosphere. Appl Opt 10(7):1600–1604, DOI 10.1364/AO.10.001600
Stawiarski C, Träumner K, Knigge C, Calhoun R (2013) Scopes and challenges of dual - Doppler lidar wind measurements - an error analysis. Journal of Atmospheric and Oceanic Technology 30(9):2044–2062, DOI 10.1175/JTECH-D-12-00244.1
Stawiarski C, Träumner K, Kottmeier C, Knigge C, Raasch S (2015) Assessment of surface-layer coherent structure detection in dual-Doppler lidar data based on virtual measurements. Boundary-Layer Meteorology 156(3):371–393, DOI 10.1007/s10546-015-0039-3
Teunissen H (1980) Structure of mean winds and turbulence in the planetary boundary layer over rural terrain. Boundary-Layer Meteorology 19(2):187–221, DOI 10.1007/BF00117220
Toriumi R, Katsuchi H, Furuya N (2000) A study on spatial correlation of natural wind. Journal of Wind Engineering and Industrial Aerodynamics 87(23):203 – 216, DOI 10.1016/S0167-6105(00)00037-4, 10th International Conference on Wind Engineering
Vickery BJ (1970) On the reliability of gust loading factors. In: Proc., Technical Meeting Concerning Wind Loads on Buildings and Structures, Building Science Series, vol 30, pp 296–312
Wang H, Li A, Niu J, Zong Z, Li J (2013) Long-term monitoring of wind characteristics at Sutong Bridge site. Journal of Wind Engineering and Industrial Aerodynamics 115:39 – 47, DOI 10.1016/j.jweia.2013.01.006
Wang H, Wu T, Tao T, Li A, Kareem A (2016) Measurements and analysis of non-stationary wind characteristics at Sutong Bridge in Typhoon Damrey. Journal of Wind Engineering and Industrial Aerodynamics 151:100 – 106, DOI 10.1016/j.jweia.2016.02.001
Welch PD (1967) The use of fast Fourier transform for the estimation of power spectra: A method based on time averaging over short, modified periodograms. IEEE Trans Audio Electroacoustics 15:70–73, DOI 10.1109/TAU.1967.1161901
Xu Y (2013) Wind Effects on Cable-Supported Bridges. Wiley